Numerical Dissipation Switch for Two-Dimensional Central-Upwind Schemes

Alexander Kurganov*, Yongle Liu† and Vladimir Zeitlin ‡

Abstract

We propose a numerical dissipation switch, which helps to control the amount of numerical dissipation present in central-upwind schemes. Our main goal is to reduce the numerical dissipation without risking oscillations. This goal is achieved with the help of a more accurate estimate of the local propagation speeds in the parts of the computational domain, which are near contact discontinuities and shears. To this end, we introduce a switch parameter, which depends on the distributions of energy in the x- and y-directions. The resulting new central-upwind is tested on a number of numerical examples, which demonstrate the superiority of the proposed method over the original central-upwind scheme.

Key words: Central-upwind schemes, numerical dissipation, local speeds of propagation, Euler equations of gas dynamics, thermal rotating shallow water equations.

AMS subject classification: 76M12, 65M08, 35L65, 86-08.

1 Introduction

We consider two-dimensional (2-D) hyperbolic systems of conservation laws, which can be written as

$$\boldsymbol{U}_t + \boldsymbol{F}(\boldsymbol{U})_x + \boldsymbol{G}(\boldsymbol{U})_y = \boldsymbol{0}, \tag{1.1}$$

where x and y are spatial variables, t is time, $\boldsymbol{U}(x,y,t) \in \mathbb{R}^d$ is the vector of unknowns, and $\boldsymbol{F}$ and $\boldsymbol{G}$ are the x- and y-fluxes, respectively.

It is well-known that numerically computing solutions of (1.1) is a challenging task since many of these solutions develop very complicated nonsmooth structures including shock waves, contact discontinuities and rarefaction zones. One of the most popular numerical tools for hyperbolic

*Department of Mathematics, Southern University of Science and Technology, Shenzhen, 518055, China and SUSTech International Center for Mathematics, Southern University of Science and Technology, Shenzhen, 518055, China; alexander@sustech.edu.cn

†Department of Mathematics, Harbin Institute of Technology, Harbin, 150001, China and Department of Mathematics, Southern University of Science and Technology, Shenzhen, 518055, China; liuyl2017@mail.sustech.edu.cn

‡Laboratoire de Météorologie Dynamique, Sorbonne Université (SU), Ecole Normale Supérieure (ENS), CNRS, Paris, 75231, France and Department of Mathematics, Southern University of Science and Technology, Shenzhen, 518055, China; zeitlin@lmd.ens.fr

systems of conservation and balance laws are finite-volume methods; see, e.g., [7,12,14–16,29,45]. Most of the finite-volume methods are designed for the one-dimensional (1-D) version of (1.1) and then extended to the higher-dimensional cases in a dimension-by-dimension manner. There are also genuinely multidimensional methods (see, e.g., [2,17,20,21,27,28,35]), which are often advantageous as they are less prone to grid effects.

In this paper, we focus on genuinely multidimensional *central-upwind* schemes, which are Riemann-problem-solver-free methods that can be applied to a wide variety of hyperbolic systems of conservation and balance laws as a robust, stable and highly accurate "black-box" solver. Central-upwind schemes were originally developed in [20,23,24] as a low dissipative alternative to staggered central schemes—the second-order Nessyahu-Tadmor scheme [37] and its multidimensional and higher-order extensions (see, e.g., [1,13,30–32]). The amount of numerical dissipation present in central-upwind scheme was reduced in [17,22]. Our goal is to further reduce the numerical dissipation by introducing a numerical dissipation switch, which is similar to the switch recently developed in [38]. We present the switch in the context of Euler equations of gas dynamics. It can be, however, used in many other models as, for instance, thermal rotating shallow water equations as it is done in Example 6 below.

The paper is organized as follows. In §2, we briefly review the semi-discrete central-upwind scheme from [3,17]. In §3, we discuss application of the scheme to the 2-D Euler equations of gas dynamics and present the numerical dissipation switch. In §4, we demonstrate the effects of the switch on a number of numerical examples.

2 Semi-Discrete Central-Upwind Scheme – Brief Overview

In this section, we briefly review the 2-D semi-discrete second-order central-upwind scheme from [3,17].

We divide the computational domain into a set of uniform Cartesian cells $C_{j,k} := [x_{j-\frac12}, x_{j+\frac12}]\times[y_{k-\frac12}, y_{k+\frac12}]$, which are centered at $(x_j, y_k) = (x_{j-\frac12}+\Delta x/2, y_{k-\frac12}+\Delta y/2)$. We assume that the solution of (1.1), realized in terms of its cell averages,

$$\overline{\boldsymbol{U}}_{j,k}(t) :\approx \frac{1}{\Delta x\Delta y}\iint\limits_{C_{j,k}} \boldsymbol{U}(x,y,t)\,\mathrm{d}x\,\mathrm{d}y,$$

is available at a certain time t. The solution is then evolved in time by solving the following system of ODEs:

$$\frac{\mathrm{d}}{\mathrm{d}t}\overline{\boldsymbol{U}}_{j,k}(t) = -\frac{\boldsymbol{\mathcal{F}}_{j+\frac12,k}(t)-\boldsymbol{\mathcal{F}}_{j-\frac12,k}(t)}{\Delta x} - \frac{\boldsymbol{\mathcal{G}}_{j,k+\frac12}(t)-\boldsymbol{\mathcal{G}}_{j,k-\frac12}(t)}{\Delta y}, \tag{2.1}$$

where $\boldsymbol{\mathcal{F}}_{j+\frac12,k}(t)$ and $\boldsymbol{\mathcal{G}}_{j,k+\frac12}(t)$ are the central-upwind numerical fluxes in the x- and y-directions, respectively.

Remark 2.1 For the sake of brevity, we will omit the dependence of all of the indexed finite-volume quantities on t in the rest of this paper.

The central-upwind numerical fluxes from [17] are

$$\begin{aligned}\boldsymbol{\mathcal{F}}_{j+\frac12,k}&=\frac{a^+_{j+\frac12,k}\boldsymbol{F}(\boldsymbol{U}^{\rm E}_{j,k})-a^-_{j+\frac12,k}\boldsymbol{F}(\boldsymbol{U}^{\rm W}_{j+1,k})}{a^+_{j+\frac12,k}-a^-_{j+\frac12,k}}+\frac{a^+_{j+\frac12,k}a^-_{j+\frac12,k}}{a^+_{j+\frac12,k}-a^-_{j+\frac12,k}}\left[\boldsymbol{U}^{\rm W}_{j+1,k}-\boldsymbol{U}^{\rm E}_{j,k}-\delta\boldsymbol{U}_{j+\frac12,k}\right],\\ \boldsymbol{\mathcal{G}}_{j,k+\frac12}&=\frac{b^+_{j,k+\frac12}\boldsymbol{G}(\boldsymbol{U}^{\rm N}_{j,k})-b^-_{j,k+\frac12}\boldsymbol{G}(\boldsymbol{U}^{\rm S}_{j,k+1})}{b^+_{j,k+\frac12}-b^-_{j,k+\frac12}}+\frac{b^+_{j,k+\frac12}b^-_{j,k+\frac12}}{b^+_{j,k+\frac12}-b^-_{j,k+\frac12}}\left[\boldsymbol{U}^{\rm S}_{j,k+1}-\boldsymbol{U}^{\rm N}_{j,k}-\delta\boldsymbol{U}_{j,k+\frac12}\right].\end{aligned}\tag{2.2}$$

Here, $\delta\boldsymbol{U}_{j+\frac12,k}$ and $\delta\boldsymbol{U}_{j,k+\frac12}$ are built-in "anti-diffusion" terms:

$$\begin{aligned}\delta\boldsymbol{U}_{j+\frac12,k}&=\text{minmod}\left(\boldsymbol{U}^{\rm SW}_{j+1,k}-\boldsymbol{U}^*_{j+\frac12,k},\,\boldsymbol{U}^*_{j+\frac12,k}-\boldsymbol{U}^{\rm SE}_{j,k},\,\boldsymbol{U}^{\rm NW}_{j+1,k}-\boldsymbol{U}^*_{j+\frac12,k},\,\boldsymbol{U}^*_{j+\frac12,k}-\boldsymbol{U}^{\rm NE}_{j,k}\right),\\ \delta\boldsymbol{U}_{j,k+\frac12}&=\text{minmod}\left(\boldsymbol{U}^{\rm SW}_{j,k+1}-\boldsymbol{U}^*_{j,k+\frac12},\,\boldsymbol{U}^*_{j,k+\frac12}-\boldsymbol{U}^{\rm NW}_{j,k},\,\boldsymbol{U}^{\rm SE}_{j,k+1}-\boldsymbol{U}^*_{j,k+\frac12},\,\boldsymbol{U}^*_{j,k+\frac12}-\boldsymbol{U}^{\rm NE}_{j,k}\right),\end{aligned}\tag{2.3}$$

where

$$\begin{aligned}\boldsymbol{U}^*_{j+\frac12,k}&=\frac{a^+_{j+\frac12,k}\boldsymbol{U}^{\rm W}_{j+1,k}-a^-_{j+\frac12,k}\boldsymbol{U}^{\rm E}_{j,k}-\left\{\boldsymbol{F}(\boldsymbol{U}^{\rm W}_{j+1,k})-\boldsymbol{F}(\boldsymbol{U}^{\rm E}_{j,k})\right\}}{a^+_{j+\frac12,k}-a^-_{j+\frac12,k}},\\ \boldsymbol{U}^*_{j,k+\frac12}&=\frac{b^+_{j,k+\frac12}\boldsymbol{U}^{\rm S}_{j,k+1}-b^-_{j,k+\frac12}\boldsymbol{U}^{\rm N}_{j,k}-\left\{\boldsymbol{G}(\boldsymbol{U}^{\rm S}_{j,k+1})-\boldsymbol{G}(\boldsymbol{U}^{\rm N}_{j,k})\right\}}{b^+_{j,k+\frac12}-b^-_{j,k+\frac12}}.\end{aligned}\tag{2.4}$$

In (2.2)–(2.4), the point values

$$\begin{aligned}\boldsymbol{U}^{\rm E}_{j,k}&=\overline{\boldsymbol{U}}_{j,k}+\frac{\Delta x}{2}(\boldsymbol{U}_x)_{j,k},\quad \boldsymbol{U}^{\rm W}_{j,k}=\overline{\boldsymbol{U}}_{j,k}-\frac{\Delta x}{2}(\boldsymbol{U}_x)_{j,k},\\ \boldsymbol{U}^{\rm N}_{j,k}&=\overline{\boldsymbol{U}}_{j,k}+\frac{\Delta y}{2}(\boldsymbol{U}_y)_{j,k},\quad \boldsymbol{U}^{\rm S}_{j,k}=\overline{\boldsymbol{U}}_{j,k}-\frac{\Delta y}{2}(\boldsymbol{U}_y)_{j,k}\end{aligned}\tag{2.5}$$

and

$$\boldsymbol{U}^{\rm NE(NW)}_{j,k}=\overline{\boldsymbol{U}}_{j,k}\pm\frac{\Delta x}{2}(\boldsymbol{U}_x)_{j,k}+\frac{\Delta y}{2}(\boldsymbol{U}_y)_{j,k},\quad \boldsymbol{U}^{\rm SE(SW)}_{j,k}=\overline{\boldsymbol{U}}_{j,k}\pm\frac{\Delta x}{2}(\boldsymbol{U}_x)_{j,k}-\frac{\Delta y}{2}(\boldsymbol{U}_y)_{j,k}\tag{2.6}$$

are to be computed using a nonlinear limiter to minimize spurious oscillations. For example, one can use the generalized minmod limiter (see, e.g., [33, 37, 44, 46]):

$$\begin{aligned}(\boldsymbol{U}_x)_{j,k}&=\text{minmod}\left(\sigma\,\frac{\overline{\boldsymbol{U}}_{j,k}-\overline{\boldsymbol{U}}_{j-1,k}}{\Delta x},\,\frac{\overline{\boldsymbol{U}}_{j+1,k}-\overline{\boldsymbol{U}}_{j-1,k}}{2\Delta x},\,\sigma\,\frac{\overline{\boldsymbol{U}}_{j+1,k}-\overline{\boldsymbol{U}}_{j,k}}{\Delta x}\right),\\ (\boldsymbol{U}_y)_{j,k}&=\text{minmod}\left(\sigma\,\frac{\overline{\boldsymbol{U}}_{j,k}-\overline{\boldsymbol{U}}_{j,k-1}}{\Delta y},\,\frac{\overline{\boldsymbol{U}}_{j,k+1}-\overline{\boldsymbol{U}}_{j,k-1}}{2\Delta y},\,\sigma\,\frac{\overline{\boldsymbol{U}}_{j,k+1}-\overline{\boldsymbol{U}}_{j,k}}{\Delta y}\right),\end{aligned}\tag{2.7}$$

where the parameter $\sigma\in[1,2]$ helps to control the smoothness of the reconstructed values (larger values of σ correspond to sharper, but more oscillatory reconstructions).

The minmod function used in (2.3) and (2.7) is defined by

$$\text{minmod}(z_1,z_2,\ldots):=\begin{cases}\min\limits_k\{z_k\}, & \text{if } z_k>0\ \forall k,\\ \max\limits_k\{z_k\}, & \text{if } z_k<0\ \forall k,\\ 0, & \text{otherwise,}\end{cases}$$

and is applied in both (2.3) and (2.7) in a component-wise manner.

Finally, $a^{\pm}_{j+\frac12,k}$ and $b^{\pm}_{j,k+\frac12}$ are the one-sided local propagation speeds, which can be estimated, for example, by

$$\begin{aligned}
a^+_{j+\frac12,k} &= \max\left\{\lambda_d\left(\frac{\partial \boldsymbol{F}}{\partial \boldsymbol{U}}\left(\boldsymbol{U}^{\rm W}_{j+1,k}\right)\right),\ \lambda_d\left(\frac{\partial \boldsymbol{F}}{\partial \boldsymbol{U}}\left(\boldsymbol{U}^{\rm E}_{j,k}\right)\right),\ 0\right\},\\
a^-_{j+\frac12,k} &= \min\left\{\lambda_1\left(\frac{\partial \boldsymbol{F}}{\partial \boldsymbol{U}}\left(\boldsymbol{U}^{\rm W}_{j+1,k}\right)\right),\ \lambda_1\left(\frac{\partial \boldsymbol{F}}{\partial \boldsymbol{U}}\left(\boldsymbol{U}^{\rm E}_{j,k}\right)\right),\ 0\right\},\\
b^+_{j,k+\frac12} &= \max\left\{\lambda_d\left(\frac{\partial \boldsymbol{G}}{\partial \boldsymbol{U}}\left(\boldsymbol{U}^{\rm S}_{j,k+1}\right)\right),\ \lambda_d\left(\frac{\partial \boldsymbol{G}}{\partial \boldsymbol{U}}\left(\boldsymbol{U}^{\rm N}_{j,k}\right)\right),\ 0\right\},\\
b^-_{j,k+\frac12} &= \min\left\{\lambda_1\left(\frac{\partial \boldsymbol{G}}{\partial \boldsymbol{U}}\left(\boldsymbol{U}^{\rm S}_{j,k+1}\right)\right),\ \lambda_1\left(\frac{\partial \boldsymbol{G}}{\partial \boldsymbol{U}}\left(\boldsymbol{U}^{\rm N}_{j,k}\right)\right),\ 0\right\},
\end{aligned} \tag{2.8}$$

where $\lambda_1 < \lambda_2 < \ldots < \lambda_d$ are the d eigenvalues of the corresponding Jacobians, $\frac{\partial \boldsymbol{F}}{\partial \boldsymbol{U}}$ and $\frac{\partial \boldsymbol{G}}{\partial \boldsymbol{U}}$.

Remark 2.2 We would like to point out that the upper bounds on the local speeds of propagation given in (2.8) may be inaccurate; see, for example, [11]. Moreover, we have implemented the strategy from [11] in Examples 1–6 below, but since it did not make any impact on the results in any of the conducted numerical experiments, we only use the straightforward estimates (2.8) in this paper.

Remark 2.3 We note that the semi-discrete central-upwind scheme (2.1)–(2.8) is a system of time dependent ODEs, which should be integrated by a sufficiently accurate, efficient and stable ODE solver. In our numerical experiments, we have used the three-stage third-order strong stability preserving (SSP) Runge-Kutta method (see, e.g., [8, 9]) with an adaptive time step computed at every time level using the CFL number 0.475:

$$\Delta t = 0.475 \min\left\{\frac{\Delta x}{a_{\max}}, \frac{\Delta y}{b_{\max}}\right\}, \tag{2.9}$$

where

$$a_{\max} := \max_{j,k}\left\{a^+_{j+\frac12,k}, -a^-_{j+\frac12,k}\right\}, \quad b_{\max} := \max_{j,k}\left\{b^+_{j,k+\frac12}, -b^-_{j,k+\frac12}\right\}. \tag{2.10}$$

3 Numerical Dissipation Switch

In this section, we present a way to reduce the amount of numerical dissipation present in the central-upwind scheme from §2 applied to the 2-D Euler equations of gas dynamics:

$$\begin{aligned}
&\rho_t + (\rho u)_x + (\rho v)_y = 0,\\
&(\rho u)_t + (\rho u^2 + p)_x + (\rho uv)_y = 0,\\
&(\rho v)_t + (\rho uv)_x + (\rho v^2 + p)_y = 0,\\
&E_t + [u(E+p)]_x + [v(E+p)]_y = 0.
\end{aligned} \tag{3.1}$$

Here, ρ is the density, u and v are the x- and y-velocities, respectively, p is the pressure, and E is the total energy, which is related to the primitive variables ρ, u, v and p via the equation of state (EOS). For the ideal gas, the EOS is

$$E = \frac{p}{\gamma - 1} + \frac{\rho}{2}\left(u^2 + v^2\right),$$

where γ is the specific heat ratio taken to be 1.4 in all of the numerical examples reported in §4.

According to (2.8), the one-sided local propagation speeds can be estimated by

$$\begin{aligned}
a^+_{j+\frac12,k} &= \max\left\{u^{\rm E}_{j,k}+c^{\rm E}_{j,k},\ u^{\rm W}_{j+1,k}+c^{\rm W}_{j+1,k},\ 0\right\},\\
a^-_{j+\frac12,k} &= \min\left\{u^{\rm E}_{j,k}-c^{\rm E}_{j,k},\ u^{\rm W}_{j+1,k}-c^{\rm W}_{j+1,k},\ 0\right\},\\
b^+_{j,k+\frac12} &= \max\left\{v^{\rm N}_{j,k}+c^{\rm N}_{j,k},\ v^{\rm S}_{j,k+1}+c^{\rm S}_{j,k+1},\ 0\right\},\\
b^-_{j,k+\frac12} &= \min\left\{v^{\rm N}_{j,k}-c^{\rm N}_{j,k},\ v^{\rm S}_{j,k+1}-c^{\rm S}_{j,k+1},\ 0\right\},
\end{aligned}\tag{3.2}$$

where $c:=\sqrt{\gamma p/\rho}$ is the speed of sound, and

$$\begin{aligned}
&u^{\rm E}_{j,k}=\frac{(\overline{\rho u})^{\rm E}_{j,k}}{\overline{\rho}^{\rm E}_{j,k}},\quad u^{\rm W}_{j+1,k}=\frac{(\overline{\rho u})^{\rm W}_{j+1,k}}{\overline{\rho}^{\rm W}_{j+1,k}},\quad u^{\rm N}_{j,k}=\frac{(\overline{\rho u})^{\rm N}_{j,k}}{\overline{\rho}^{\rm N}_{j,k}},\quad u^{\rm S}_{j,k+1}=\frac{(\overline{\rho u})^{\rm S}_{j,k+1}}{\overline{\rho}^{\rm S}_{j,k+1}},\\
&v^{\rm E}_{j,k}=\frac{(\overline{\rho v})^{\rm E}_{j,k}}{\overline{\rho}^{\rm E}_{j,k}},\quad v^{\rm W}_{j+1,k}=\frac{(\overline{\rho v})^{\rm W}_{j+1,k}}{\overline{\rho}^{\rm W}_{j+1,k}},\quad v^{\rm N}_{j,k}=\frac{(\overline{\rho v})^{\rm N}_{j,k}}{\overline{\rho}^{\rm N}_{j,k}},\quad v^{\rm S}_{j,k+1}=\frac{(\overline{\rho v})^{\rm S}_{j,k+1}}{\overline{\rho}^{\rm S}_{j,k+1}},\\
&p^{\rm E}_{j,k}=(\gamma-1)\left[\overline{E}^{\rm E}_{j,k}-\frac{\overline{\rho}^{\rm E}_{j,k}}{2}\left(\left(u^{\rm E}_{j,k}\right)^2+\left(v^{\rm E}_{j,k}\right)^2\right)\right],\\
&p^{\rm W}_{j+1,k}=(\gamma-1)\left[\overline{E}^{\rm W}_{j+1,k}-\frac{\overline{\rho}^{\rm W}_{j+1,k}}{2}\left(\left(u^{\rm W}_{j+1,k}\right)^2+\left(v^{\rm W}_{j+1,k}\right)^2\right)\right],\\
&p^{\rm N}_{j,k}=(\gamma-1)\left[\overline{E}^{\rm N}_{j,k}-\frac{\overline{\rho}^{\rm N}_{j,k}}{2}\left(\left(u^{\rm N}_{j,k}\right)^2+\left(v^{\rm N}_{j,k}\right)^2\right)\right],\\
&p^{\rm S}_{j,k+1}=(\gamma-1)\left[\overline{E}^{\rm S}_{j,k+1}-\frac{\overline{\rho}^{\rm S}_{j,k+1}}{2}\left(\left(u^{\rm S}_{j,k+1}\right)^2+\left(v^{\rm S}_{j,k+1}\right)^2\right)\right],\\
&c^{\rm E}_{j,k}=\sqrt{\frac{\gamma p^{\rm E}_{j,k}}{\overline{\rho}^{\rm E}_{j,k}}},\quad c^{\rm W}_{j+1,k}=\sqrt{\frac{\gamma p^{\rm W}_{j+1,k}}{\overline{\rho}^{\rm W}_{j+1,k}}},\quad c^{\rm N}_{j,k}=\sqrt{\frac{\gamma p^{\rm N}_{j,k}}{\overline{\rho}^{\rm N}_{j,k}}},\quad c^{\rm S}_{j,k+1}=\sqrt{\frac{\gamma p^{\rm S}_{j,k+1}}{\overline{\rho}^{\rm S}_{j,k+1}}}.
\end{aligned}$$

The estimate (3.2), however, may be very inaccurate in certain situations. In order to illustrate this, let us consider a particular example with the initial data that correspond to a stationary shear flow. Let us set up the discrete initial data in such a way that the boundary between the two parts of the fluid moving in the positive and negative y-directions is located at $x=x_{J+\frac12}$ for a certain index J; see Figure 3.1. One can easily verify that for this data setting

$$\boldsymbol{\mathcal{G}}_{j,k+\frac12}-\boldsymbol{\mathcal{G}}_{j,k-\frac12}=0,\ \ \forall(j,k),\quad \boldsymbol{\mathcal{F}}_{j+\frac12,k}-\boldsymbol{\mathcal{F}}_{j+\frac12,k}=0,\ \ \forall j\neq J\text{ and }j\neq J+1,\ \forall k.$$

Let us compute $\boldsymbol{\mathcal{F}}_{J-\frac12,k}$, $\boldsymbol{\mathcal{F}}_{J+\frac12,k}$ and $\boldsymbol{\mathcal{F}}_{J+\frac32,k}$. To this end, we first use (3.2) to obtain the corresponding one-sided local speeds of propagation:

$$a^-_{J-\frac12,k}=a^+_{J-\frac12,k}-=a^-_{J+\frac12,k}=-2,\quad a^+_{J+\frac12,k}=a^-_{J-\frac32,k}=a^+_{J-\frac32,k}-=1,\quad\forall k,$$

and then use them to compute the numerical fluxes, which are

$$\boldsymbol{\mathcal{F}}_{J-\frac12,k}=(0,1,0,0)^\top,\quad \boldsymbol{\mathcal{F}}_{J+\frac12,k}=(-7/15,1,14/15,0)^\top,\quad \boldsymbol{\mathcal{F}}_{J+\frac32,k}=(0,1,0,0)^\top.$$

As one can see, the initial equilibrium will not be preserved at the discrete level as $\overline{\rho}_J$, $\overline{\rho}_{J+1}$, $(\overline{\rho v})_J$ and $(\overline{\rho v})_{J+1}$ will change after the first time step. We note that this occurs precisely because of the discrepancy between $a^-_{J+\frac12,k}$ and $a^+_{J+\frac12,k}$ values caused by a very inaccurate overestimate of the local speeds, which, in turn, leads to excessive numerical dissipation in the shear area.

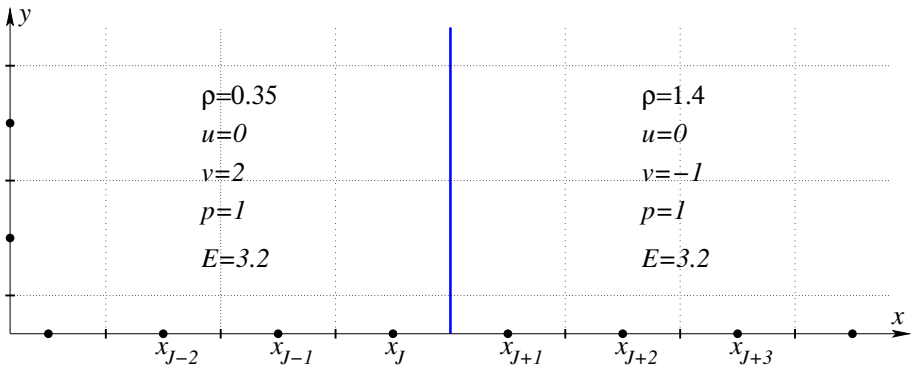

Figure 3.1: Initial setting for a stationary shear flow.

Therefore, in order to improve the resolution of the central-upwind scheme, we develop a numerical dissipation switch, which will help to better estimate the one-sided local propagation speeds by reducing the magnitudes of $a^\pm_{j+\frac12,k}$ and/or $b^\pm_{j,k+\frac12}$ in the areas where the solution is near contact discontinuities and shears. By doing this, we will reduce the size of the control volumes used for the evolution of the solution in those areas (see [17] for details on the derivation of central-upwind schemes via the integral form of conservation laws) and thus reduce the amount of numerical dissipation there. At the same time, we will keep a sufficient amount of numerical dissipation near shock waves to guarantee the stability of the method. To this end, we follow the approach in [38] and add a switch on the sound speed parts of the estimates in (3.2), which are replaced by

$$\begin{aligned}
a^+_{j+\frac12,k} &= \max\left\{u^{\rm E}_{j,k}+\alpha_{j+\frac12,k}c^{\rm E}_{j,k},\ u^{\rm W}_{j+1,k}+\alpha_{j+\frac12,k}c^{\rm W}_{j+1,k},\ 0\right\},\\
a^-_{j+\frac12,k} &= \min\left\{u^{\rm E}_{j,k}-\alpha_{j+\frac12,k}c^{\rm E}_{j,k},\ u^{\rm W}_{j+1,k}-\alpha_{j+\frac12,k}c^{\rm W}_{j+1,k},\ 0\right\},\\
b^+_{j,k+\frac12} &= \max\left\{v^{\rm N}_{j,k}+\beta_{j,k+\frac12}c^{\rm N}_{j,k},\ v^{\rm S}_{j,k+1}+\beta_{j,k+\frac12}c^{\rm S}_{j,k+1},\ 0\right\},\\
b^-_{j,k+\frac12} &= \min\left\{v^{\rm N}_{j,k}-\beta_{j,k+\frac12}c^{\rm N}_{j,k},\ v^{\rm S}_{j,k+1}-\beta_{j,k+\frac12}c^{\rm S}_{j,k+1},\ 0\right\},
\end{aligned}\tag{3.3}$$

where $\alpha_{j+\frac12,k}\in[0,1]$ and $\beta_{j,k+\frac12}\in[0,1]$ are the switch parameters designed to be small near contact discontinuities and shears. This goal is achieved by setting

$$\alpha_{j+\frac12,k}=\begin{cases}\dfrac{\Delta\alpha^{(1)}_{j+\frac12,k}}{\Delta\alpha_{j+\frac12,k}}, & \text{if } \Delta\alpha_{j+\frac12,k}>\varepsilon,\\ 0, & \text{otherwise,}\end{cases}\tag{3.4}$$

where

$$\begin{aligned}
\Delta\alpha^{(1)}_{j+\frac12,k} &= \left|\frac{p^{\rm W}_{j+1,k}-p^{\rm E}_{j,k}}{\gamma-1}+\frac{\rho^{\rm W}_{j+1,k}(u^{\rm W}_{j+1,k})^2-\rho^{\rm E}_{j,k}(u^{\rm E}_{j,k})^2}{2}\right|,\\
\Delta\alpha^{(2)}_{j+\frac12,k} &= \left|\frac{\rho^{\rm W}_{j+1,k}(v^{\rm W}_{j+1,k})^2-\rho^{\rm E}_{j,k}(v^{\rm E}_{j,k})^2}{2}\right|, \quad \Delta\alpha_{j+\frac12,k}=\sqrt{\left(\Delta\alpha^{(1)}_{j+\frac12,k}\right)^2+\left(\Delta\alpha^{(2)}_{j+\frac12,k}\right)^2}.
\end{aligned} \tag{3.5}$$

The motivation behind (3.3)–(3.5) is based on the observation that in the case when $\alpha^{(1)}_{j+\frac12,k}$ is much smaller than $\alpha^{(2)}_{j+\frac12,k}$, the local speed of propagation in the x-direction at the boundary between cells $C_{j,k}$ and $C_{j+1,k}$ is determined by the intermediate eigenvalue u rather than by $u+c$ and $u-c$.

Similarly, the switch in the y-direction is constructed using

$$\beta_{j,k+\frac12}=\begin{cases}\dfrac{\Delta\beta^{(1)}_{j,k+\frac12}}{\Delta\beta_{j,k+\frac12}}, & \text{if } \Delta\beta_{j,k+\frac12}>\varepsilon,\\ 0, & \text{otherwise,}\end{cases} \tag{3.6}$$

where

$$\begin{aligned}
\Delta\beta^{(1)}_{j,k+\frac12} &= \left|\frac{p^{\rm S}_{j,k+1}-p^{\rm N}_{j,k}}{\gamma-1}+\frac{\rho^{\rm S}_{j,k+1}(v^{\rm S}_{j,k+1})^2-\rho^{\rm N}_{j,k}(v^{\rm N}_{j,k})^2}{2}\right|,\\
\Delta\beta^{(2)}_{j,k+\frac12} &= \left|\frac{\rho^{\rm S}_{j,k+1}(u^{\rm S}_{j,k+1})^2-\rho^{\rm N}_{j,k}(u^{\rm N}_{j,k})^2}{2}\right|, \quad \Delta\beta_{j,k+\frac12}=\sqrt{\left(\Delta\beta^{(1)}_{j,k+\frac12}\right)^2+\left(\Delta\beta^{(2)}_{j,k+\frac12}\right)^2}.
\end{aligned}$$

In (3.4) and (3.6), ε is a small positive parameter designed to prevent division by zero.

Let us now turn back to the example with the initial setting outlined in Figure 3.1. It is easy to verify that after we replace the one-sided local speeds (3.2) with (3.3)–(3.5), all of the local speeds in the x-direction will reduce to $a^{\pm}_{j+\frac12}\equiv 0$ and the initial steady state will be exactly preserved at the discrete level. This simple example is designed to illustrate the main idea of the proposed switch. Its advantages will be further demonstrated in a variety of numerical examples in §4.

Remark 3.1 In order to minimize the risk of instability, we use the values $a^{\pm}_{j+\frac12,k}$ and $b^{\pm}_{j,k+\frac12}$ estimated in (3.2) (rather than their reduced versions given by (3.3)) in the computation of the time steps in (2.9) and (2.10).

4 Numerical Examples

In this section, we demonstrate the performance of the proposed semi-discrete second-order central-upwind scheme with numerical dissipation switch on several numerical examples. In all of the experiments, we take the minmod parameter $\sigma=1.3$ and the switch threshold parameter $\varepsilon=10^{-12}$.

In the remaining part of the paper, we will refer to the proposed central-upwind scheme with the switch as "NEW scheme", while the original central-upwind scheme will be referred to as "OLD scheme".

Example 1 — Moving Contact Wave

In the first example, we numerically capture an isolated moving contact wave to compare the performance of the NEW and OLD schemes. To this end, we consider a 2-D contact wave on the computational domain $\Omega = [-0.2, 0.2] \times [0, 0.8]$ with free boundary conditions and the initial data given by

$$\big(\rho(x,y,0), u(x,y,0), v(x,y,0), p(x,y,0)\big)^\top = \begin{cases} (1.4, 0, 0.2, 1)^\top, & (x,y) \in D, \\ (1.0, 0, 0.2, 1)^\top, & \text{otherwise.} \end{cases}$$

Here, the domain D, outlined using the dashed line in Figure 4.3, consists of the points $(x, y) \in \Omega$ that satisfy the following conditions:

$$\{-0.1 < x < 0.1,\ 0 < y < 0.02\} \bigcup \{-0.02 < x < 0.02,\ 0.02 < y < 0.1\} \bigcup$$
$$\big\{(x+0.02)^2 + (y-0.02)^2 < 0.08^2\big\} \bigcup \big\{(x-0.02)^2 + (y-0.02)^2 < 0.08^2\big\}.$$

We first proceed with the numerical simulations using the first-order scheme, which is obtained by replacing the point values given by (2.5) and (2.6) with the corresponding cell averages:

$$\boldsymbol{U}^{\rm E}_{j,k} = \boldsymbol{U}^{\rm W}_{j,k} = \boldsymbol{U}^{\rm N}_{j,k} = \boldsymbol{U}^{\rm S}_{j,k} = \boldsymbol{U}^{\rm NE}_{j,k} = \boldsymbol{U}^{\rm NW}_{j,k} = \boldsymbol{U}^{\rm SE}_{j,k} = \boldsymbol{U}^{\rm SW}_{j,k} = \overline{\boldsymbol{U}}_{j,k}, \quad \forall (j,k).$$

The results (density) computed on the uniform grid with $\Delta x = \Delta y = 2/500$ at the final time $t = 2$ for both the NEW and OLD schemes are plotted in Figure 4.1. As one can clearly see, the proposed numerical dissipation switch helps to significantly reduce the numerical dissipation, especially at the contact waves (located at $x = \pm 0.1$), which are drastically smeared by the OLD scheme. This can be also clearly seen in Figure 4.2, where we plot the 1-D slices of the computed solutions along the lines $x = 0.07$ and $y = 0.21$.

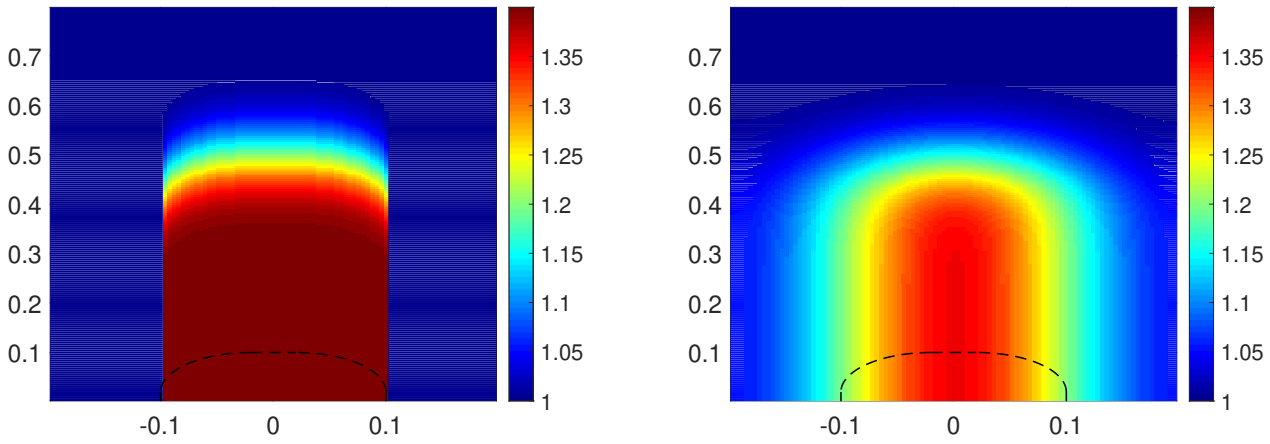

Figure 4.1: Example 1: Density (ρ) computed by the first-order versions of the NEW (left) and OLD (right) schemes. The dashed line represents the initial contact line.

We then use the second-order schemes and plot the obtained results in Figure 4.3. As one can observe, the contact wave, especially its parts located along the lines $x = \pm 0.1$, captured much more accurately by the NEW scheme. This is confirmed in Figure 4.4, where we plot the 1-D slices of the computed solutions along the lines $x = 0.07$ and $y = 0.21$.

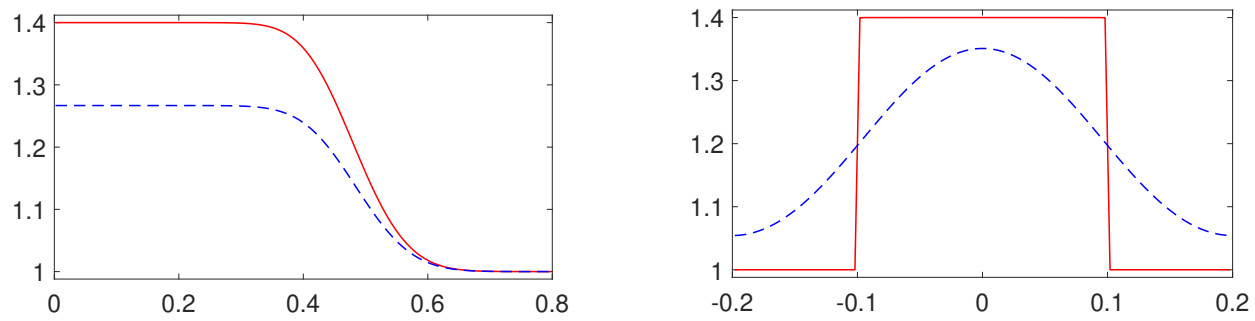

Figure 4.2: Example 1: 1-D slices along the lines $x = 0.07$ (left) and $y = 0.21$ (right) of the density (ρ) computed by the first-order versions of the NEW (solid lines) and OLD (dashed lines) schemes.

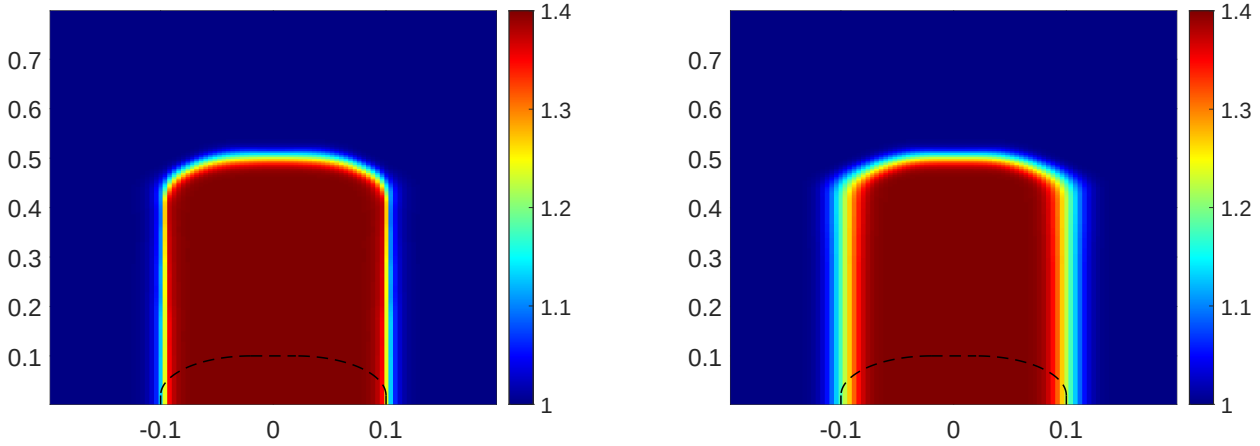

Figure 4.3: Example 1: Same as Figure 4.1 but for the second-order schemes.

Example 2 — Two-Dimensional Riemann problem

In the second example, we consider the 2-D Riemann problems and test the proposed central-upwind scheme on all of the 19 configurations[1] from [24]; see also [26, 41, 42, 49]. The obtained results demonstrate the robustness of the NEW scheme that generates the numerical solutions, which are not more oscillatory than the solutions computed by the OLD scheme or the central-upwind schemes from [24]. At the same time, the reduced numerical dissipation helps to improve the resolution of some parts of the computed solution. In order to illustrate this, we plot in Figure 4.5 the densities computed in Configurations 11, 13, 17 and 19. As one can see, there are some improvements achieved by the NEW scheme, especially in the resolution of contact waves.

We also perform a more detailed numerical study for one of the configurations—Configuration 3, considered in a slightly larger computational domain $[0, 1.2] \times [0, 1.2]$ discretized using about

[1]These are genuinely different admissible configurations for polytropic gas, separated by the three types of 1-D centered waves, namely, rarefaction, shock and contact waves.

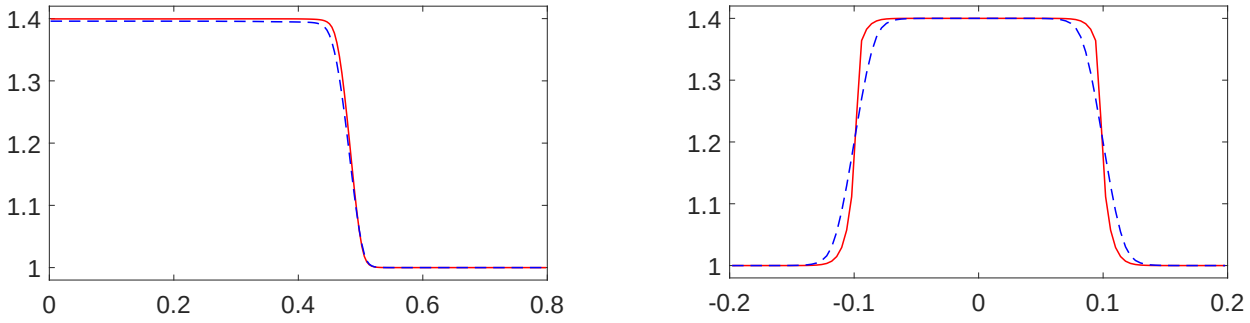

Figure 4.4: Example 1: Same as Figure 4.2 but for the second-order schemes.

twice finer mesh with 1000×1000 uniform cells. The boundary conditions are the zero-order extrapolation and the initial data are given by

$$\big(\rho,u,v,p\big)^\top=\begin{cases}(1.5,0,0,1.5)^\top, & x>1,y>1,\\ (0.5323,1.206,0,0.3)^\top, & x<1,y>1,\\ (0.1380,1.206,1.206,0.029)^\top, & x<1,y<1,\\ (0.5323,0,1.206,0.3)^\top, & x>1,y<1.\end{cases}$$

We compute the solutions until the final time $t=1$ and then plot the densities computed by the NEW and OLD schemes in Figure 4.6 (top row). As one can clearly see, both schemes maintain the diagonal symmetry of the guitar-like shape of the jet. However, we can clearly see that the NEW scheme, unlike the OLD one, captures a sideband instability of the jet, expected in the zones of strong along-jet velocity shear; see Figure 4.6 (bottom row), where we plot the velocity field.

It is instructive to take a look at the final time distributions of the switch parameters $\alpha_{j+\frac{1}{2},k}$ and $\beta_{j,k+\frac{1}{2}}$, which are plotted in Figure 4.7. As one can observe, the parameters vary between 0 and 1 and their distributions clearly reflect the structure of the computed density shown in Figure 4.6 (left).

Example 3 — Explosion

In the third example, which is taken from [34], the initial conditions are radially symmetric and given by

$$\big(\rho(x,y,0),u(x,y,0),v(x,y,0),p(x,y,0)\big)^\top=\begin{cases}(1.000,0,0,1.0)^\top, & x^2+y^2<0.16,\\ (0.125,0,0,0.1)^\top, & \text{otherwise.}\end{cases}$$

The computational domain is $[0,1.5]\times[0,1.5]$. It is well-known (see, e.g., [5,17,22,34]) that the computed circular contact curve should develop instability by the time $t=3.2$ unless the numerical

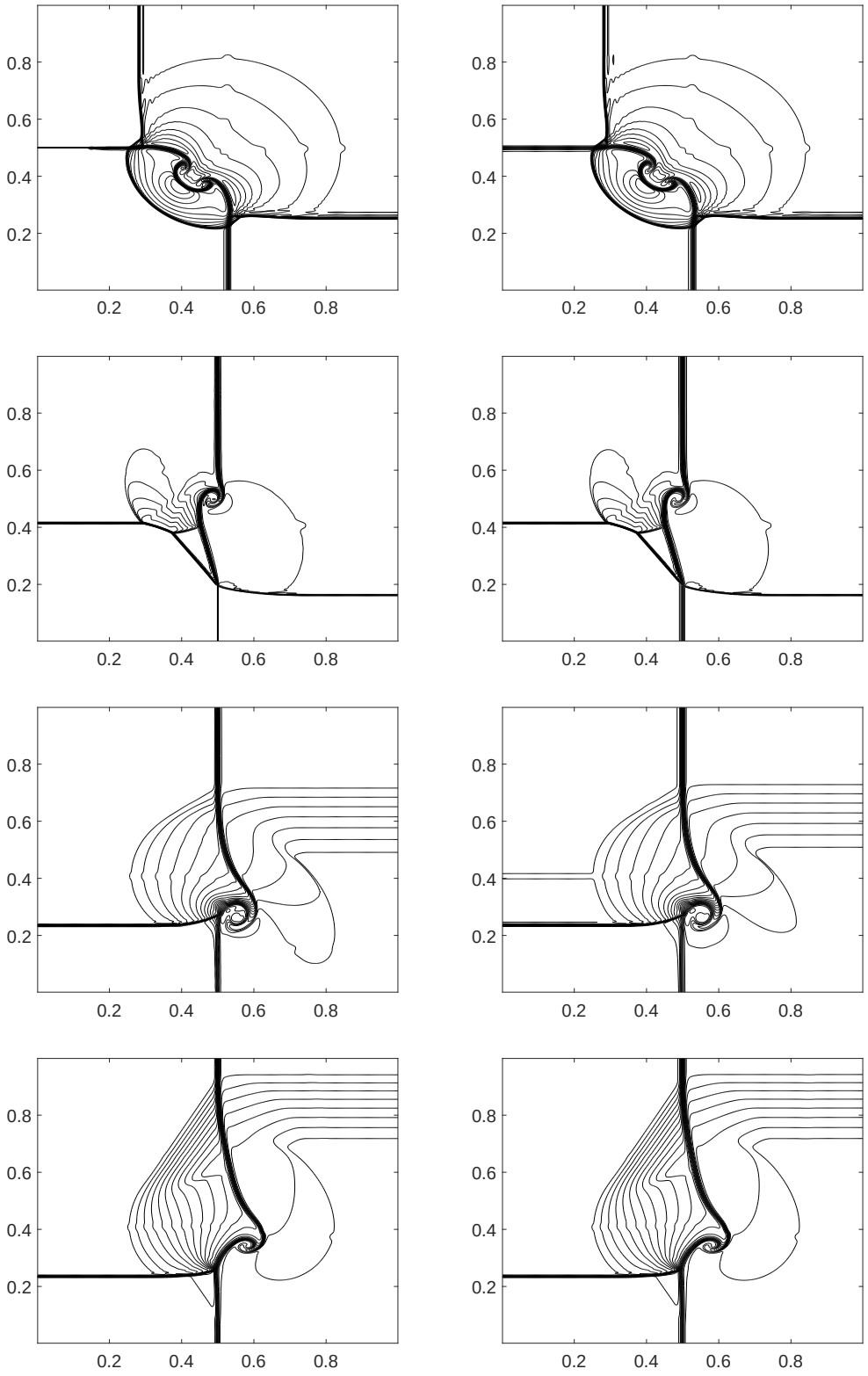

Figure 4.5: Example 2: Densities (ρ) computed by the NEW (left column) and OLD (right column) schemes. From top to bottom: Configurations 11, 13, 17 and 19. The initial settings, final times ($t = 0.3$) and mesh size (400×400 cells in the $[0, 1] \times [0, 1]$ computational domain) are identical to those used in [24].

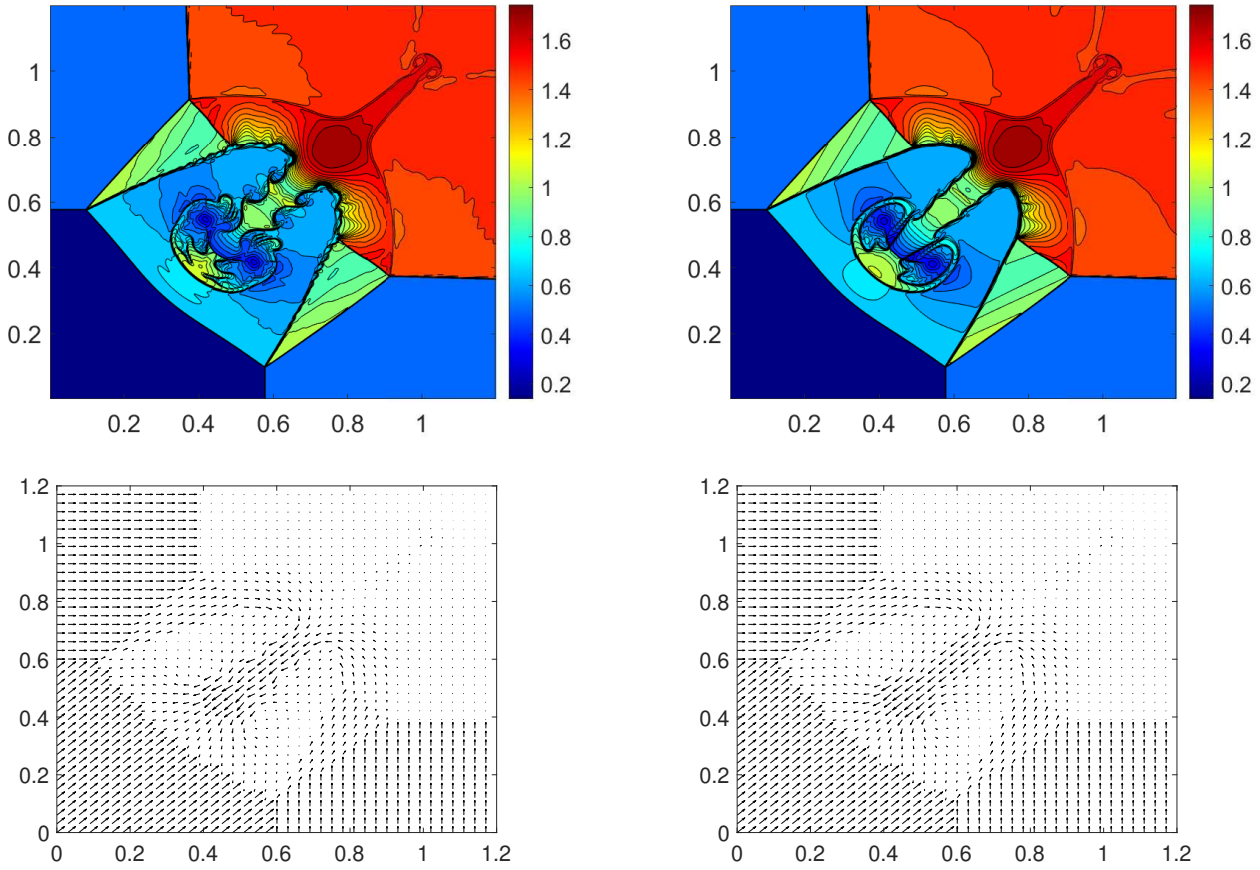

Figure 4.6: Example 2, Configuration 3: Density (top row) and velocity field (bottom row) computed by the NEW (left column) and OLD (right column) schemes.

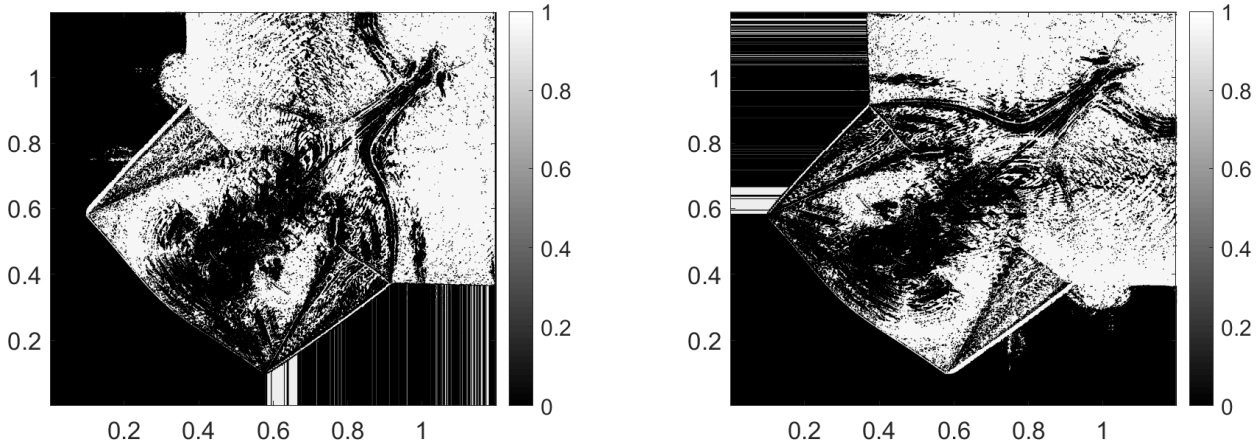

Figure 4.7: Example 2, Configuration 3: Switch parameters $\alpha_{j+\frac{1}{2},k}$ (left) and $\beta_{j,k+\frac{1}{2}}$ (right).

method contains an excessive amount of numerical dissipation. Therefore, this is a good test to compare the numerical dissipation present in the NEW and OLD schemes.

We solve the underlying problem using the uniform mesh with $\Delta x = \Delta y = 3/800$ and set reflecting boundary conditions at $x = 0$ and $y = 0$ and free boundary conditions at $x = 1.5$ and $y = 1.5$. The ρ-component of the solutions obtained at time $t = 3.2$ are plotted in Figure 4.8. As one can see there, the contact surface computed by the NEW scheme is much "curlier" than the one computed by the OLD scheme. This demonstrates that the use of numerical dissipation switch helps to reduce the amount of numerical dissipation present in the central-upwind scheme. The final time distributions of the switch parameters $\alpha_{j+\frac{1}{2},k}$ and $\beta_{j,k+\frac{1}{2}}$ are plotted in Figure 4.9. Note that a small reduction in the numericall dissipation does not lead to any instabilities in the neighborhood of the circular shock wave.

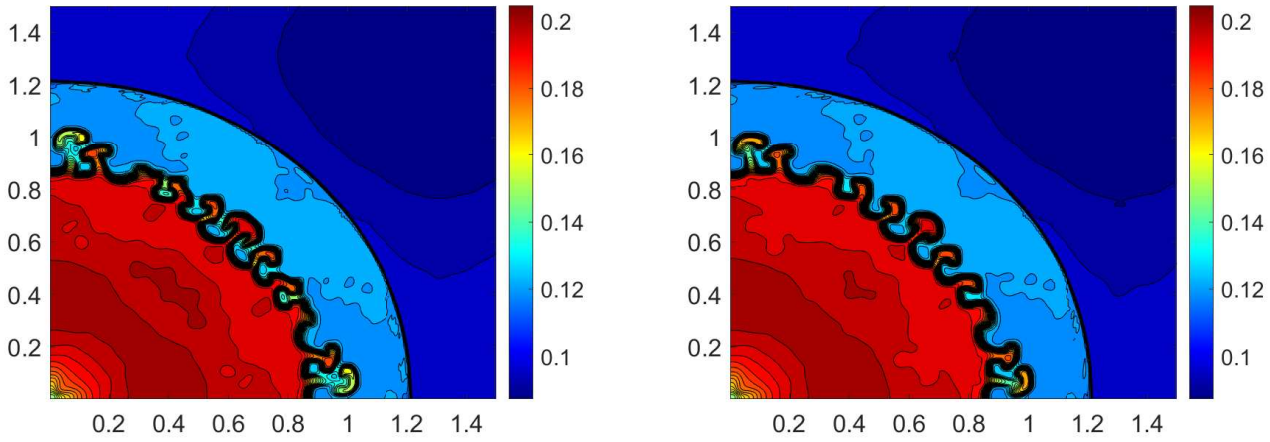

Figure 4.8: Example 3: Density (ρ) computed by the NEW (left) and OLD (right) schemes.

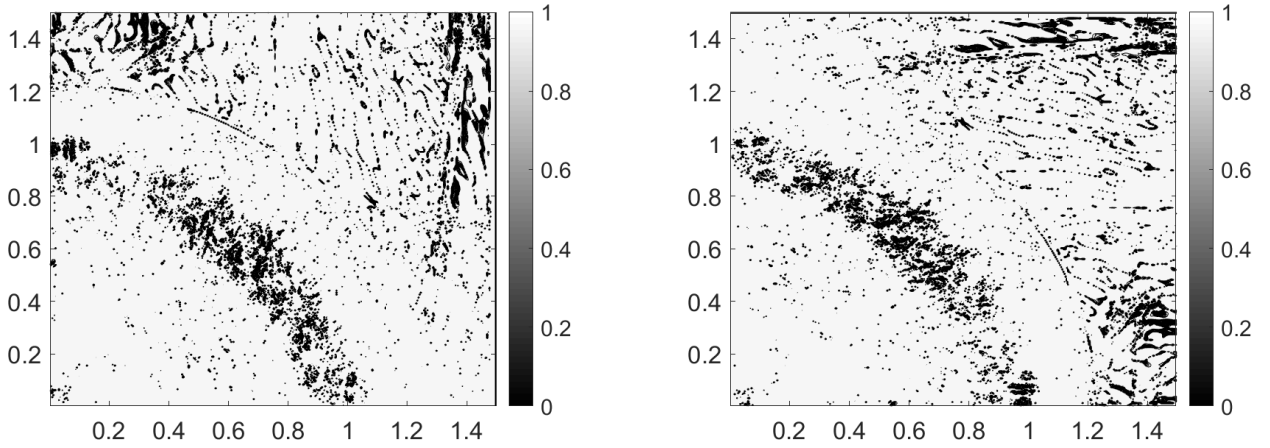

Figure 4.9: Example 3: Switch parameters $\alpha_{j+\frac{1}{2},k}$ (left) and $\beta_{j,k+\frac{1}{2}}$ (right).

Example 4 — Implosion

In the fourth example, also taken from [34], we numerically solve the implosion problem in a square domain $[0, 0.3]\times[0, 0.3]$ and with solid wall boundary conditions. This test case is a challenging one

because of the presence of non-grid-aligned shocks and emergence of a jet. The initial conditions are:

$$\big(\rho(x,y,0),u(x,y,0),v(x,y,0),p(x,y,0)\big)^\top=\begin{cases}(0.125,0,0,0.14)^\top, & |x|+|y|<0.15,\\ (1.000,0,0,1.00)^\top, & \text{otherwise.}\end{cases}$$

We first compute the solution on the uniform grid with $\Delta x=\Delta y=3/6000$ until the final time $t=2.5$. As demonstrated in [34] (also see [5,22]), a jet of fluid is expected to emerge. This can be seen in the upper row of Figure 4.10, where the jet produced by the NEW scheme develops faster, which indicates a lower amount of numerical dissipation present in this scheme. Moreover, if we refine the mesh by taking $\Delta x=\Delta y=3/8000$, then the computed jets propagate further towards the center of the computational domain (as the amount of numerical dissipation reduces when the mesh is refined), but the NEW scheme is still clearly less dissipative than the OLD one; see the lower row of Figure 4.10.

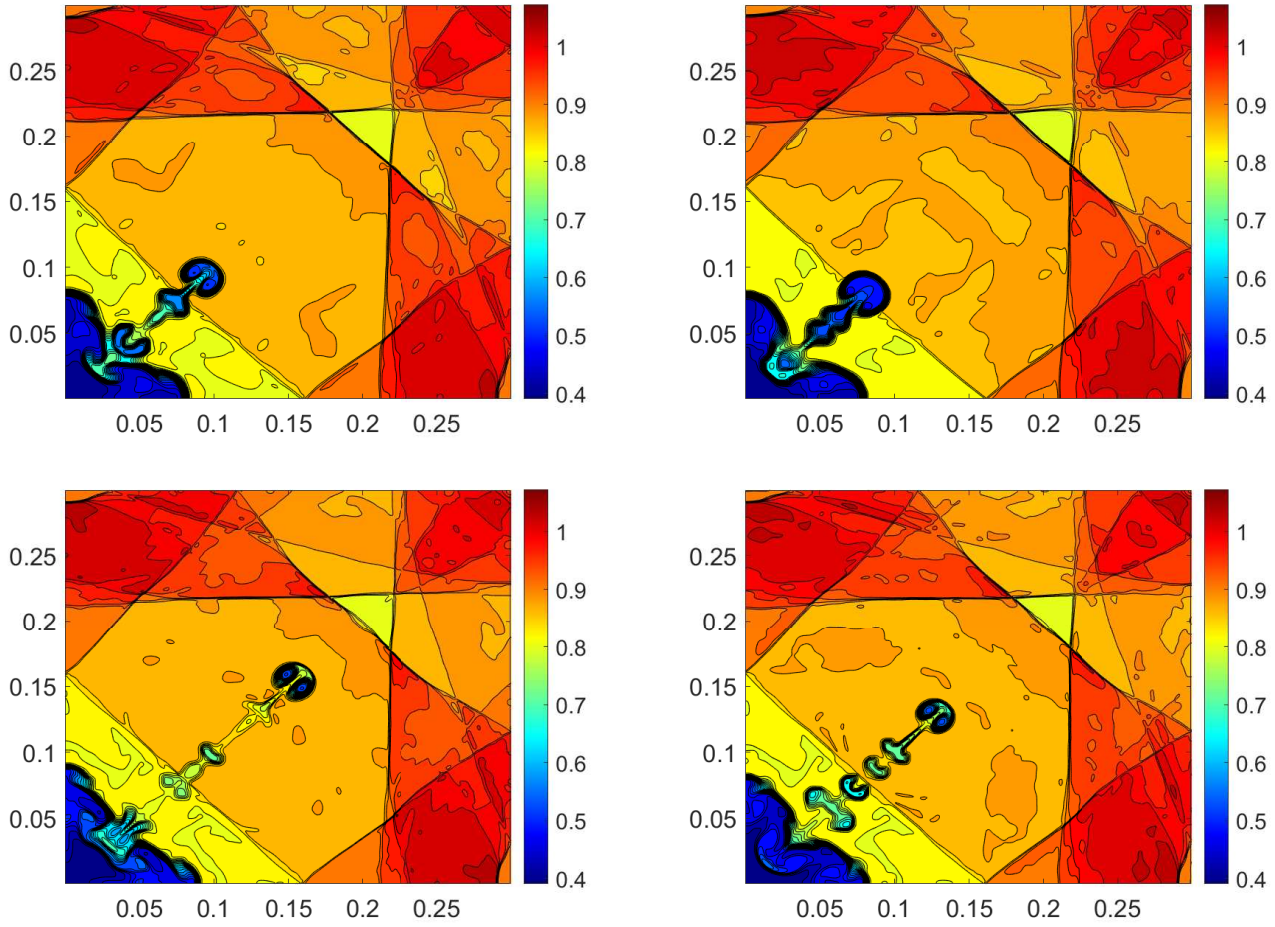

Figure 4.10: Example 4: Density (ρ) computed by the NEW (left column) and OLD (right column) schemes using a coarser (with $\Delta x=\Delta y=3/6000$; upper row) and finer (with $\Delta x=\Delta y=3/8000$; lower row) meshes.

Example 5 — Kelvin-Helmholtz (KH) Instability

In the fifth example, we numerically study the KH instability, which is taken from [38], and also studied in [6]. The KH instability occurs when a shearing flow is slightly perturbed and it will generate internal waves, which are growing, breaking and forming vortices. This is the reason why we can see some beautiful breaking wave-like cloud patterns or billow clouds in the sky. Here, we study the KH instability to demonstrate that the NEW scheme has much better ability to capture the formation of a wave pattern then the OLD one. To this end, we consider the following initial conditions in [38]:

$$\big(\rho(x,y,0),u(x,y,0)\big)=\begin{cases}\big(1,-0.5+0.5e^{(y+0.25)/L}\big), & y\in[-0.5,-0.25),\\ \big(2,0.5-0.5e^{(-y-0.25)/L}\big), & y\in[-0.25,0),\\ \big(2,0.5-0.5e^{(y-0.25)/L}\big), & y\in[0,0.25),\\ \big(1,-0.5+0.5e^{(0.25-y)/L}\big), & y\in[0.25,0.5],\end{cases}$$

where L is a smoothing parameter and we take $L=0.00625$ corresponding to a thin shear interface in the simulation below. Besides, the initial pressure $p(x,y,0)=1.5$ and the vertical velocity is

$$v(x,y,0)=0.01\sin(4\pi x).$$

The computation domain is $[-0.5,0.5]\times[-0.5,0.5]$. We use a uniform grid with $\Delta x=\Delta y=1/1024$ and the periodic boundary conditions to compute the solutions until time $t=4$. The slices of density ρ at times $t=1$, 2.5 and 4 are plotted in Figure 4.11. We can clearly see that, at $t=1$, the NEW scheme capture slightly more vortices than the OLD one, especially the small wavy bumps at the position around $(-0.15,0.26)$, $(0.35,0.26)$, $(-0.42,-0.28)$ and $(0.07,-0.28)$. From these four positions, we observe that the NEW scheme produce more clear swirl structures. At later time $t=2.5$, the difference between the proposed NEW scheme and the OLD scheme is apparently obvious. As one can see, the NEW scheme resolves secondary instabilities of KH billows and resolves more details in the wave-breaking pattern, among other things. However, these are much more fuzzy when computed by the OLD scheme. Furthermore, one can observe that the vortices produced by the NEW scheme move faster than the those captured by the OLD scheme. At the final time $t=4$, we can first see that the results of the NEW scheme are much less diffusive, as the red color is much darker which corresponding low-dissipation results. Second, we find that the NEW scheme produces more isolated and complicated vorticities indicating that this scheme can capture the KH instability much better than the OLD one. The time evolution of the switch parameters $\alpha_{j+\frac{1}{2},k}$ and $\beta_{j,k+\frac{1}{2}}$ is shown in Figure 4.12, where one can see that the parameters near the rapidly changing parts of the solution are less than 1, which helps to reduce the numerical diffusion there.

Example 6 — Raleigh-Taylor (RT) Instability

In this example, we numerically investigate the RT instability, which is a common test for accuracy studies of numerical schemes and contains both discontinuities and complex flow structure. Instead of (3.1), we include a source terms acting downward in the y-direction. In fact, we solve the

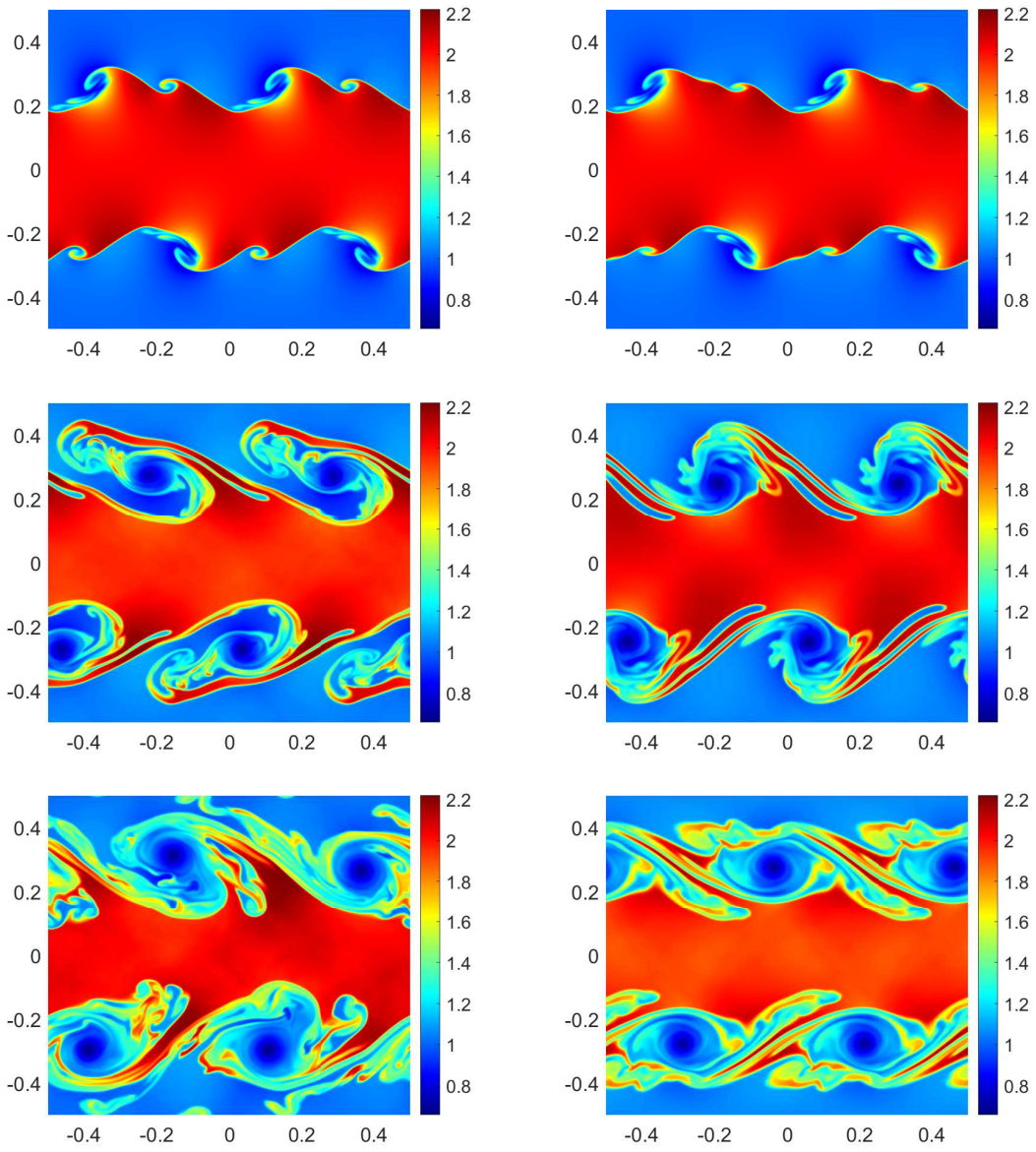

Figure 4.11: Example 5: Density (ρ) computed by the NEW (left column) and OLD (right column) schemes at times $t = 1$ (top row), 2.5 (middle row) and 4 (bottom row).

following 2-D system:

$$\begin{aligned}
&\rho_t + (\rho u)_x + (\rho v)_y = 0,\\
&(\rho u)_t + (\rho u^2 + p)_x + (\rho uv)_y = 0,\\
&(\rho v)_t + (\rho uv)_x + (\rho v^2 + p)_y = \rho,\\
&E_t + [u(E + p)]_x + [v(E + p)]_y = \rho v.
\end{aligned}$$

We follow the setting in [43] and consider the following initial conditions:

$$(\rho, u, v, p)(x, y, 0) = \begin{cases} (2, 0, -0.025\, c\cos(8\pi x), 2y + 1), & y < 0.5,\\ (1, 0, -0.025\, c\cos(8\pi x), y + 1), & \text{otherwise,} \end{cases}$$

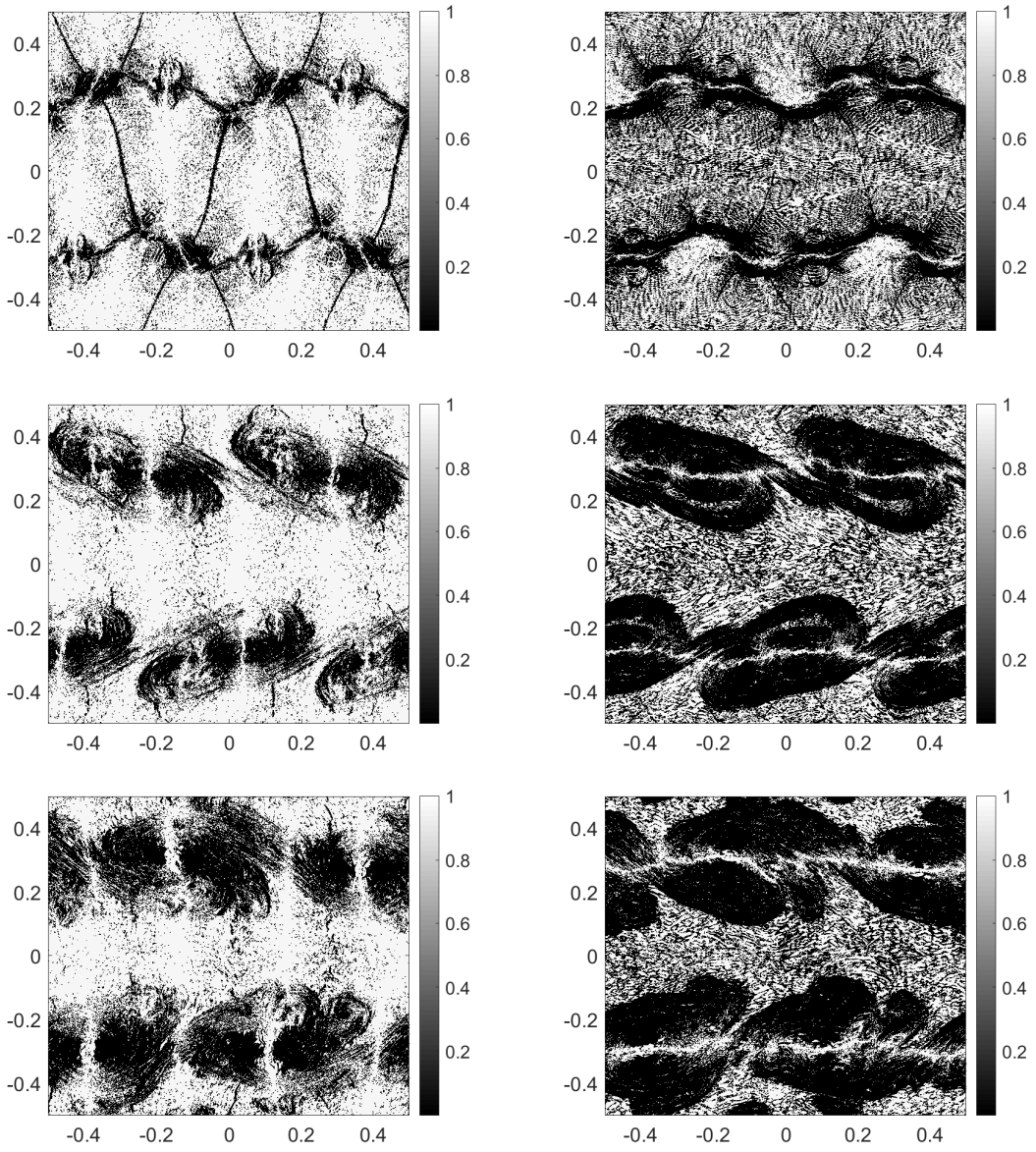

Figure 4.12: Example 5: Switch parameters $\alpha_{j+\frac{1}{2},k}$ (left column) and $\beta_{j,k+\frac{1}{2}}$ (right column) at times $t = 1$ (top row), 2.5 (middle row) and 4 (bottom row).

where $c = \sqrt{\frac{\gamma p}{\rho}}$ is the sound speed. We should remark that in this example, we take the ratio of specific heats $\gamma = \frac{5}{3}$. The computation is prescribed in the domain $[0, 1/4] \times [0, 1]$ and reflective boundary conditions on left and right border lines are imposed. In addition, top and bottom boundary states are fixed to $(1, 0, 0, 2.5)$ and $(2, 0, 0, 1)$, respectively.

This test is a useful one to verify numerical methods, as the resolution and richness of vortical structures of this test case can be utilized as a measure of the numerical dissipation introduced by the methods. In Figure 4.13, we use $\Delta x = \Delta y = 1/1024$ to compare the solutions computed by the above two schemes at the times $t = 1.95$ and 2.95, respectively. As one can see, at earlier time $t = 1.95$, there are no obvious differences between two schemes. However, at later time $t = 2.95$, the difference is so obvious that we can clearly see the NEW scheme gives a much

better resolution in complicated solution structures than the OLD one with same mesh size. It demonstrates that the more dissipative OLD scheme suppresses the Rayleigh-Taylor instability and artificially stabilizes the contact surface, while the NEW scheme can obtain the higher resolution for the complicated flow structure. Finally, the time evolution of the switch parameters $\alpha_{j+\frac{1}{2},k}$ and $\beta_{j,k+\frac{1}{2}}$, presented in Figure 4.14, clearly demonstrates that these parameters are self-adapted to the developing structures of the computed solution.

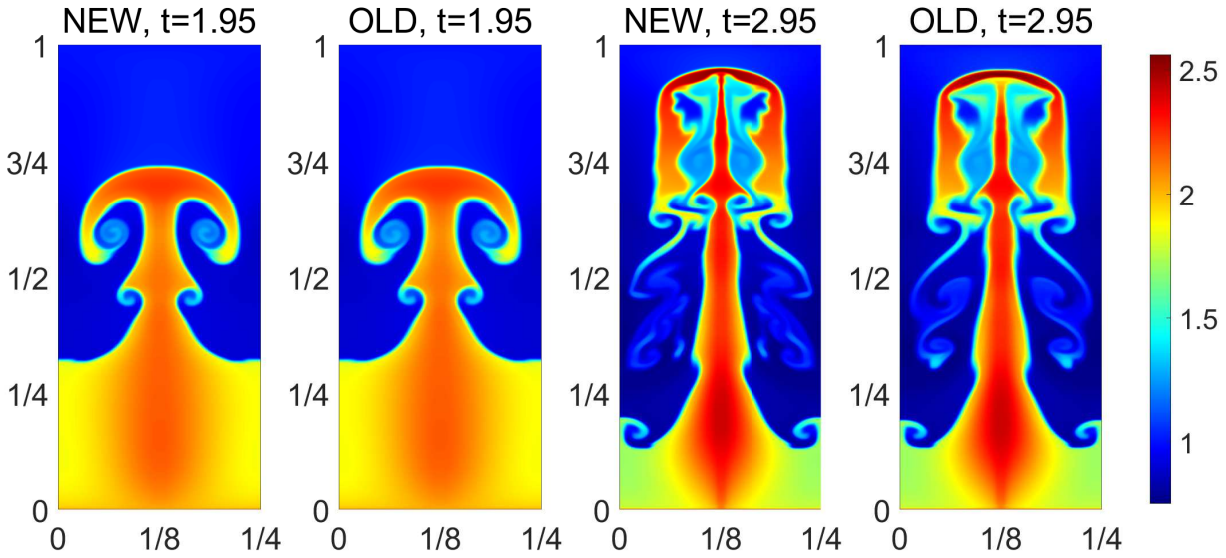

Figure 4.13: Example 6: Density (ρ) computed by the NEW and OLD schemes.

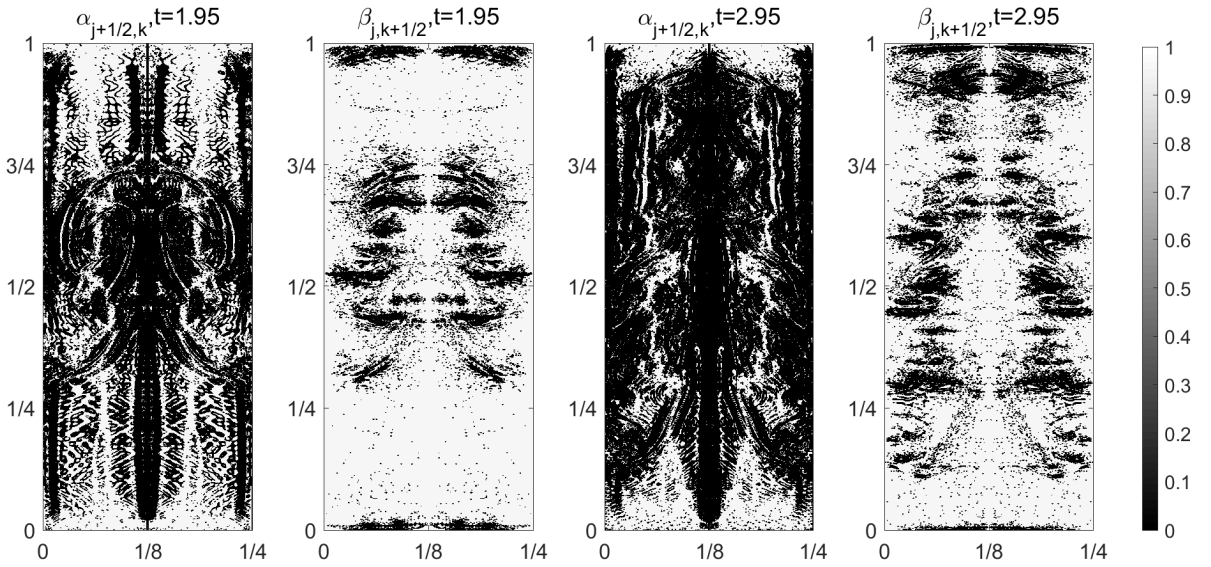

Figure 4.14: Example 6: Switch parameters $\alpha_{j+\frac{1}{2},k}$ and $\beta_{j,k+\frac{1}{2}}$.

Remark 4.1 In order to numerically preserve the symmetry property of the computational results, in our experiments we rewrite the initial velocity in the y-direction in the following symmetric

form:

$$v(x,y,0)=\begin{cases}-0.025\,c\cos(8\pi x), & \text{if } x<0.125,\\ -0.025\,c\cos\big(8\pi(0.25-x)\big), & \text{otherwise.}\end{cases}$$

Example 7 — Vortex Instability in Thermal Rotating Shallow Water Equations

In this example, we consider the 2-D thermal rotating shallow water equations (see [18, 19]):

$$\begin{aligned}&h_t+(hu)_x+(hv)_y=0,\\ &(hu)_t+(hu^2+\frac{\theta}{2}h^2)_x+(huv)_y=fhv+h\theta Z_x,\\ &(hv)_t+(huv)_x+(hv^2+\frac{\theta}{2}h^2)_y=-fhu-h\theta Z_y,\\ &(h\theta)_t+(hu\theta)_x+(hv\theta)_y=0,\end{aligned}\tag{4.1}$$

which was repeatedly rediscovered and used in the literature both in the atmospheric and oceanic context; see, e.g., [4, 25, 36, 39, 40, 47, 48]. In (4.1), h denotes the thickness of the fluid layer, Z represents the bottom topography, u and v stand for the zonal and meridional velocities, respectively, θ is the relative potential temperature, and $f(y)$ is the Coriolis parameter and taken to be $f(y)\equiv 1$ in this example.

We consider the vortex instability test, which was introduced in [10] as a benchmark crash test for numerical schemes; see [10, 18] for more details. The initial conditions are given by

$$h(r,0)\equiv 1,\quad \theta(r,0)=1-\frac{1}{5}\int\limits_r^\infty\Big(1+\frac{V(r')}{10r'}\Big)\,\mathrm{d}r',\quad u(r,0)=-\frac{y}{r}V(r),\quad v(r,0)=\frac{x}{r}V(r),\tag{4.2}$$

where $r=\sqrt{x^2+y^2}$, and $V(r)=r\exp\big(-(r^3-1)/3\big)$ is the nondimensional velocity. We note that the unperturbed vortex (4.2) does not preserve its initial structure for very long time and thus one cannot clearly see the appearance of instability. We therefore follow the approach in [10, 18] and superimpose the purely thermal vortex with an unstable mode with azimuthal wavenumber $n=3$ and a small amplitude of the order of one percent of the background vortex field. In Figure 4.15, we plot the relative potential temperature θ computed by the NEW and OLD schemes in the computational domain $[-3,3]\times[-3,3]$ at times $t=100$, 150, 200 and 250. We notice that, at an earlier time $t=100$, one cannot see any visible difference between the results obtained by the both schemes. However, at later times $t=150$, 200 and 250, one can clearly see that the NEW scheme produces more complicated branches than the OLD one, and the difference between the solutions computed by the two studied schemes becomes more and more obvious as time increases. Furthermore, the inertial instabilities develop much faster and become more evident in the NEW scheme results.

On the other hand, in order to see the advantages of the NEW scheme in a more quantitative way, we compute the standard deviation of the potential temperature θ from its initial value:

$$\mathcal{S}(t)=\sqrt{\frac{1}{N_xN_y}\sum_{j=1}^{N_x}\sum_{k=1}^{N_y}\Big[\theta_{j,k}(t)-\theta_{j,k}(0)\Big]^2},\tag{4.3}$$

where $N_x \times N_y$ is a number of computational cells. We expect that the less-dissipative NEW scheme will produce a larger standard deviation as the less-dissipative solution is expected to develop more complex structures. In Figure 4.16, we plot $\mathcal{S}(t)$ computed by the NEW and OLD schemes using coarser and finer uniform meshes with $\Delta x = \Delta y = 1/100$ and $\Delta x = \Delta y = 1/150$, respectively. As one can clearly see, higher resolution solutions indeed have larger standard deviation. We also observe that the solutions computed by the NEW scheme have larger standard deviation than the ones computed by the OLD scheme on the same mesh. This demonstrates that the NEW scheme indeed has the reduced amount of numerical dissipation.

Remark 4.2 A detailed information about the thermal rotating shallow water equations, flux globalization based central-upwind scheme for them, and the corresponding numerical dissipation switch can be found in [18, 19]. In Example 7, we only illustrate the effect of the numerical dissipation switch.

Acknowledgment: The work of A. Kurganov was supported in part by NSFC grant 11771201 and by the fund of the Guangdong Provincial Key Laboratory of Computational Science and Material Design (No. 2019B030301001). The work of A. Kurganov and V. Zeitlin was supported in part by the French National Program LEFE.

References

[1] P. Arminjon, M.-C. Viallon, and A. Madrane, *A finite volume extension of the Lax-Friedrichs and Nessyahu-Tadmor schemes for conservation laws on unstructured grids*, Int. J. Comput. Fluid Dyn., 9 (1997), pp. 1–22.

[2] D. S. Balsara and B. Nkonga, *Multidimensional Riemann problem with self-similar internal structure—part III—a multidimensional analogue of the HLLI Riemann solver for conservative hyperbolic systems*, J. Comput. Phys., 346 (2017), pp. 25–48.

[3] A. Chertock, S. Cui, A. Kurganov, Ş. N. Özcan, and E. Tadmor, *Well-balanced schemes for the Euler equations with gravitation: Conservative formulation using global fluxes*, J. Comput. Phys., 358 (2018), pp. 36–52.

[4] D. P. Dempsey and R. Rotunno, *Topographic generation of mesoscale vortices in mixed-layer models*, J. Atmos. Sci., 45 (1988), pp. 2961–2978.

[5] J. Dewar, A. Kurganov, and M. Leopold, *Pressure-based adaption indicator for compressible Euler equations*, Numer. Methods Partial Differential Equations, 31 (2015), pp. 1844–1874.

[6] U. S. Fjordholm, S. Mishra, and E. Tadmor, *On the computation of measure-valued solutions*, Acta Numer., 25 (2016), pp. 567–679.

[7] E. Godlewski and P.-A. Raviart, *Numerical approximation of hyperbolic systems of conservation laws*, vol. 118 of Applied Mathematical Sciences, Springer-Verlag, New York, 1996.

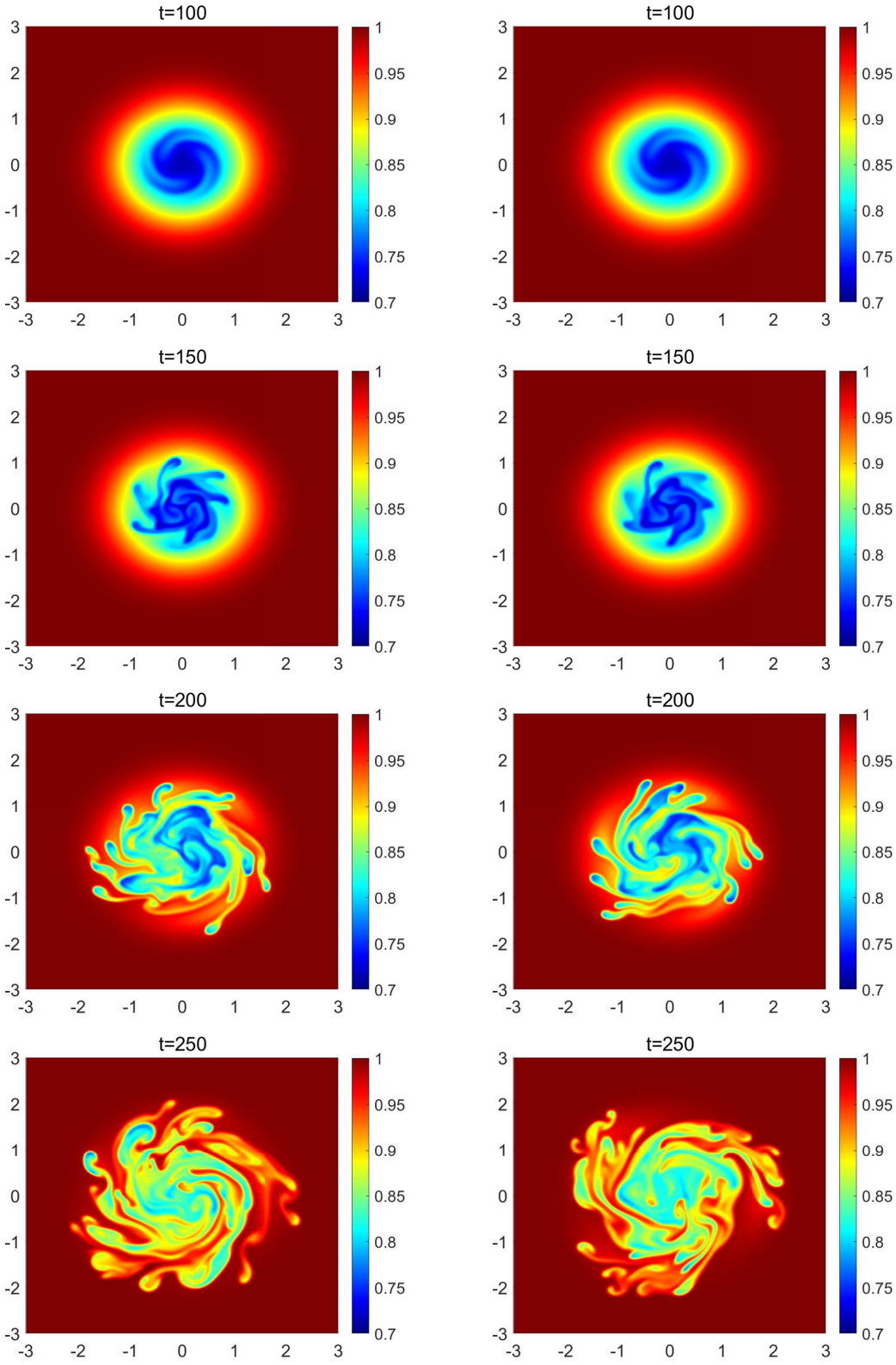

Figure 4.15: Example 7: Time snapshots of buoyancy (θ) computed by the NEW scheme (left) and OLD scheme (right) using $\Delta x = \Delta y = 1/100$ and Neumann boundary conditions.

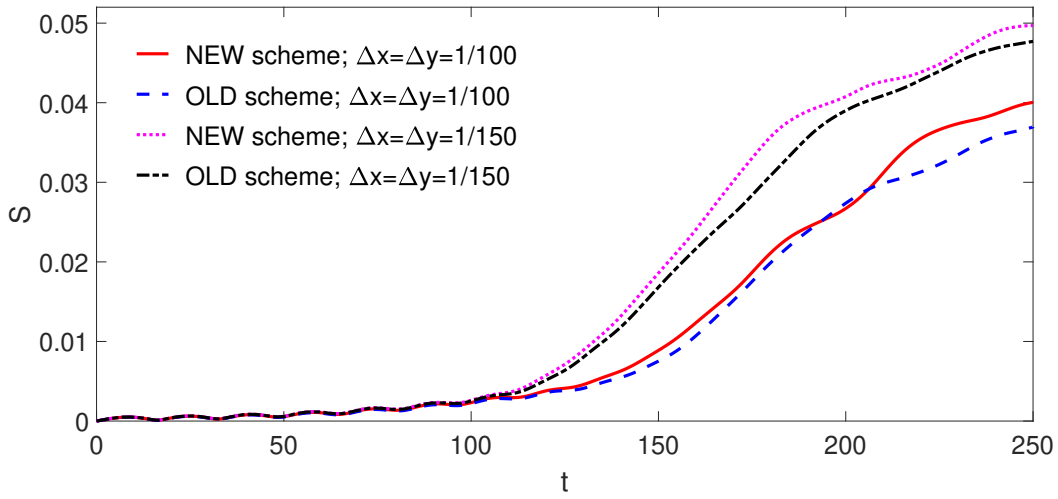

Figure 4.16: Example 7: The standard deviation $\mathcal{S}(t)$ defined in (4.3) and computed by the NEW and OLD schemes using two different uniform meshes.

[8] S. GOTTLIEB, D. KETCHESON, AND C.-W. SHU, *Strong stability preserving Runge-Kutta and multistep time discretizations*, World Scientific Publishing Co. Pte. Ltd., Hackensack, NJ, 2011.

[9] S. GOTTLIEB, C.-W. SHU, AND E. TADMOR, *Strong stability-preserving high-order time discretization methods*, SIAM Rev., 43 (2001), pp. 89–112.

[10] E. GOUZIEN, N. LAHAYE, V. ZEITLIN, AND T. DUBOS, *Thermal instability in rotating shallow water with horizontal temperature/density gradients*, Phys. Fluids, 29 (2017), p. 101702.

[11] J.-L. GUERMOND AND B. POPOV, *Fast estimation from above of the maximum wave speed in the Riemann problem for the Euler equations*, J. Comput. Phys., 321 (2016), pp. 908–926.

[12] J. S. HESTHAVEN, *Numerical methods for conservation laws*, vol. 18 of Computational Science & Engineering, Society for Industrial and Applied Mathematics (SIAM), Philadelphia, PA, 2018. From analysis to algorithms.

[13] G.-S. JIANG AND E. TADMOR, *Nonoscillatory central schemes for multidimensional hyperbolic conservation laws*, SIAM J. Sci. Comput., 19 (1998), pp. 1892–1917 (electronic).

[14] D. KRÖNER, *Numerical schemes for conservation laws*, Wiley-Teubner Series Advances in Numerical Mathematics, John Wiley & Sons Ltd., Chichester, 1997.

[15] A. KURGANOV, *Central schemes: a powerful black-box solver for nonlinear hyperbolic PDEs*, in Handbook of numerical methods for hyperbolic problems, vol. 17 of Handb. Numer. Anal., Elsevier/North-Holland, Amsterdam, 2016, pp. 525–548.

[16] ——, *Finite-volume schemes for shallow-water equations*, Acta Numer., 27 (2018), pp. 289–351.

[17] A. Kurganov and C.-T. Lin, *On the reduction of numerical dissipation in central-upwind schemes*, Commun. Comput. Phys., 2 (2007), pp. 141–163.

[18] A. Kurganov, Y. Liu, and V. Zeitlin, *Thermal vs isothermal rotating shallow water equations: comparison of dynamical processes in two models by simulations with a novel well-balanced central-upwind scheme*, Geophys. Astro. Fliud. To appear.

[19] ——, *A well-balanced central-upwind scheme for the thermal rotating shallow water equations*, J. Comput. Phys., 411 (2020), p. 109414.

[20] A. Kurganov, S. Noelle, and G. Petrova, *Semidiscrete central-upwind schemes for hyperbolic conservation laws and Hamilton-Jacobi equations*, SIAM J. Sci. Comput., 23 (2001), pp. 707–740.

[21] A. Kurganov and G. Petrova, *A third-order semi-discrete genuinely multidimensional central scheme for hyperbolic conservation laws and related problems*, Numer. Math., 88 (2001), pp. 683–729.

[22] A. Kurganov, M. Prugger, and T. Wu, *Second-order fully discrete central-upwind scheme for two-dimensional hyperbolic systems of conservation laws*, SIAM J. Sci. Comput., 39 (2017), pp. A947–A965.

[23] A. Kurganov and E. Tadmor, *New high-resolution central schemes for nonlinear conservation laws and convection-diffusion equations*, J. Comput. Phys., 160 (2000), pp. 241–282.

[24] ——, *Solution of two-dimensional riemann problems for gas dynamics without Riemann problem solvers*, Numer. Methods Partial Differential Equations, 18 (2002), pp. 584–608.

[25] R. L. Lavoie, *A mesoscale numerical model of lake-effect storms*, J. Atmos. Sci., 29 (1972), pp. 1025–1040.

[26] P. D. Lax and X.-D. Liu, *Solution of two-dimensional Riemann problems of gas dynamics by positive schemes*, SIAM J. Sci. Comput., 19 (1998), pp. 319–340 (electronic).

[27] R. J. LeVeque, *High resolution finite volume methods on arbitrary grids via wave propagation*, J. Comput. Phys., 78 (1988), pp. 36–63.

[28] ——, *Wave propagation algorithms for multi-dimensional hyperbolic systems*, J. Comput. Phys., 131 (1997), pp. 327–353.

[29] ——, *Finite volume methods for hyperbolic problems*, Cambridge Texts in Applied Mathematics, Cambridge University Press, Cambridge, 2002.

[30] D. Levy, G. Puppo, and G. Russo, *Central WENO schemes for hyperbolic systems of conservation laws*, M2AN Math. Model. Numer. Anal., 33 (1999), pp. 547–571.

[31] ——, *Compact central WENO schemes for multidimensional conservation laws*, SIAM J. Sci. Comput., 22 (2000), pp. 656–672 (electronic).

[32] ——, *A fourth-order central WENO scheme for multidimensional hyperbolic systems of conservation laws*, SIAM J. Sci. Comput., 24 (2002), pp. 480–506.

[33] K.-A. LIE AND S. NOELLE, *On the artificial compression method for second-order nonoscillatory central difference schemes for systems of conservation laws*, SIAM J. Sci. Comput., 24 (2003), pp. 1157–1174.

[34] R. LISKA AND B. WENDROFF, *Comparison of several difference schemes on 1d and 2d test problems for the euler equations*, SIAM J. Sci. Comput, 25 (2003).

[35] M. LUKÁČOVÁ-MEDVIĎOVÁ, K. W. MORTON, AND G. WARNECKE, *Finite volume evolution Galerkin methods for hyperbolic systems*, SIAM J. Sci. Comput., 26(1) (2004), pp. 1–30.

[36] J. P. MCCREARY, P. K. KUNDU, AND R. L. MOLINARI, *A numerical investigation of dynamics, thermodynamics and mixed-layer processes in the Indian Ocean*, Prog. Oceanog., 31 (1993), pp. 181–244.

[37] H. NESSYAHU AND E. TADMOR, *Nonoscillatory central differencing for hyperbolic conservation laws*, J. Comput. Phys., 87 (1990), pp. 408–463.

[38] J. PANUELOS, J. WADSLEY, AND N. KEVLAHAN, *Low shear diffusion central schemes for particle methods*. Preprint.

[39] P. RIPA, *On improving a one-layer ocean model with thermodynamics*, J. Fluid Mech., 303 (1995), pp. 169–201.

[40] M. L. SALBY, *Deep circulations under simple classes of stratification*, Tellus, 41A (1989), pp. 48–65.

[41] C. W. SCHULZ-RINNE, *Classification of the Riemann problem for two-dimensional gas dynamics*, SIAM J. Math. Anal., 24 (1993), pp. 76–88.

[42] C. W. SCHULZ-RINNE, J. P. COLLINS, AND H. M. GLAZ, *Numerical solution of the Riemann problem for two-dimensional gas dynamics*, SIAM J. Sci. Comput., 14 (1993), pp. 1394–1394.

[43] J. SHI, Y.-T. ZHANG, AND C.-W. SHU, *Resolution of high order WENO schemes for complicated flow structures*, J. Comput. Phys., 186 (2003), pp. 690–696.

[44] P. K. SWEBY, *High resolution schemes using flux limiters for hyperbolic conservation laws*, SIAM J. Numer. Anal., 21 (1984), pp. 995–1011.

[45] E. F. TORO, *Riemann solvers and numerical methods for fluid dynamics: A practical introduction*, Springer-Verlag, Berlin, Heidelberg, third ed., 2009.

[46] B. VAN LEER, *Towards the ultimate conservative difference scheme. V. A second-order sequel to Godunov's method*, J. Comput. Phys., 32 (1979), pp. 101–136.

[47] W. R. YOUNG, *The subinertial mixed layer approximation*, J. Phys. Oceanogr., 24 (1994), pp. 1812–1826.

[48] V. ZEITLIN, *Geophysical Fluid Dynamics: Understanding (almost) Everything with Rotating Shallow Water Models*, Oxford University Press, Oxford, 2018.

[49] Y. ZHENG, *Systems of conservation laws*, Progress in Nonlinear Differential Equations and their Applications, 38, Birkhäuser Boston, Inc., Boston, MA, 2001. Two-dimensional Riemann problems.